

Scaling Analysis of Multilevel Interconnect Temperatures for High-Performance ICs

Sungjun Im, *Student Member, IEEE*, Navin Srivastava, *Student Member, IEEE*,
Kaustav Banerjee, *Senior Member, IEEE*, and Kenneth E. Goodson, *Associate, IEEE*

Abstract—This paper presents a comprehensive thermal scaling analysis of multilevel interconnects in deep nanometer scale CMOS technologies based on technological, structural, and material data from the International Technology Roadmap for Semiconductors. Numerical simulations have been performed using three-dimensional electrothermal finite element methods, combined with accurate calculations of temperature- and size-dependent Cu resistivity and thermal conductivity of low- κ interlayer dielectrics (ILD) based on fully physical models. The simulations also incorporate various scaling factors from fundamental material level to system level: the via-density-dependent effective ILD thermal conductivity, the hierarchically varying root mean square current stress based on SPICE simulations, and the thermal resistance of flip-chip package. It is shown that even after considering densely embedded vias, the interconnect temperature is expected to increase significantly with scaling, due to increasing current density, increasing surface and grain boundary contributions to metal resistivity, and decreasing ILD thermal conductivity.

Index Terms—Electrothermal analysis, interconnects, Joule heating, low- κ dielectrics, metal resistivity, size effect, temperature scaling, very large-scale integrated system (VLSI), via effect.

I. INTRODUCTION

ACCURATE estimates of multilevel interconnect temperatures are necessary for interconnect performance and reliability assessment in high-performance very large-scale integrated (VLSI) circuits [1]–[3]. While some analytical thermal models are available for multilevel interconnects, the complicated multidimensional heat conduction within the three-dimensional (3-D) interconnect structures are either neglected or treated approximately [4]–[7]. Previous thermal simulations for multilevel interconnects often assumed simplified structures with arbitrary dimensions and material systems: all parallel lines in SiO₂ or polyimide [8] and only three- to four-level orthogonal wires in SiO₂ [9], [10]. Rigorous thermal analysis of multilevel interconnects must consider complex 3-D thermal coupling caused by orthogonal interconnect arrays, densely embedded vias, increasing number of metal levels, material property variations, and nonuniform current stress conditions.

This paper significantly improves upon our previous work [11] by including temperature- and size-dependent Cu resistivity,

Manuscript received June 7, 2005; revised September 16, 2005. The review of this paper was arranged by Editor V. R. Rao.

S. Im and K. E. Goodson are with the Departments of Materials Science and Engineering and Mechanical Engineering, Stanford University, Stanford, CA 94305 USA (e-mail: sjim@stanford.edu; goodson@stanford.edu).

N. Srivastava and K. Banerjee are with the Department of Electrical and Computer Engineering, University of California, Santa Barbara, CA 93106 USA (e-mail: navins@ece.ucsb.edu; kaustav@ece.ucsb.edu).

Digital Object Identifier 10.1109/TED.2005.859612

effective ILD thermal conductivity accounting for both varying via densities and via Joule heating, package thermal resistance scaling for high I/O chips, and realistic metal-level-dependent root mean square current stress inputs. The predictions made for interconnect temperatures can be used for investigating highly coupled electrothermal phenomena resulting from material property and physical parameter scaling dictated by technology evolutions. These results can also be used for enhancing backend thermal management, performance, and reliability, and for incorporating thermal-awareness in interconnect design issues such as power/ground distribution network and clock design.

The paper is organized as follows. Section II examines the scaling physics of Cu resistivity and low- κ thermal conductivity. Section III addresses detailed methodologies for the accurate simulations based on finite element methods (FEM) including via density and flip-chip package effects. In Section IV, a scaling analysis of the multilevel interconnect temperature is presented along with discussion. Finally, concluding remarks are made in Section V.

II. MATERIAL PROPERTY SCALING

A. Cu Resistivity

The metal resistivity increase due to size effects is an emerging concern as the width of on-chip interconnects approaches the mean-free path of electrons (about 40 nm for Cu at room temperature). The compact analytical model in [12] is used to calculate the resistivity of rectangular wires, which is based on the Fuchs–Sondheimer model [13], [14] regarding surface scattering and the Mayadas–Shatzkes model [15] regarding grain boundary scattering of electrons

$$\rho = \rho_o \left\{ \frac{\frac{1}{3}}{\left[\frac{1}{3} - \frac{\alpha}{2} + \alpha^2 - \alpha^3 \ln \left(1 + \frac{1}{\alpha} \right) \right]} + \frac{3}{8} C (1-p) \frac{1+AR}{AR} \frac{\lambda}{w} \right\}$$

$$\alpha = \left(\frac{\lambda}{d_g} \right) \left[\frac{R}{(1-R)} \right] \quad (1)$$

where ρ_o is the bulk resistivity, λ is the mean free path of electrons, w is the metal width, AR is the aspect ratio (height over width), p is the specularity parameter, R is the reflectivity coefficient at grain boundaries, d_g is the average distance between grain boundaries, and C is a constant (1.2 for rectangular cross sections). The accuracy of this model compared to the integral

expression used in [16] is better than 3.5% for $50 \text{ nm} < w < 1000 \text{ nm}$ [12].

In bulk materials, the grain-boundary contribution to the resistivity is small because the grain size is usually much larger than the mean free path of electrons. However, the grain size is reduced in thin films and wires, which is comparable to or smaller than the mean free path [15]. Therefore, electron scattering at the grain boundaries must be considered in wires as well as scattering at the external surfaces. The grain size in narrow Cu wires fabricated by an electrochemical process is limited by the lateral dimensions of wires and shown to increase linearly with the metal width for $w < 230 \text{ nm}$ and $\text{AR} > 1$ [12]. Therefore, d_g can be replaced by w in (1) for calculating the resistivity of metal wires based on the International Technology Roadmap for Semiconductors (ITRS) ($w = 22\text{--}185 \text{ nm}$, $\text{AR} = 1.9\text{--}2.7$). It is important to note that w and AR in (1) correspond to the actual conducting area of Cu, which excludes highly resistive thin barrier layers at the bottom and the side walls of the Cu conductor. The technology roadmap predicts that the barrier layer occupies a significant fraction of the drawn metal area: 22–23% for metal 1 (M1), 18–19% for intermediate wires, and 12% for global wires. Therefore, the barrier layer effect must be included in resistivity calculations by using corrected w and AR from the ITRS specified drawn wire dimensions and barrier layer thickness. Other parameters are average values based on [12]: $\rho_o = 2.04 \mu\Omega \cdot \text{cm}$ (300 K), $\lambda = 37.3 \text{ nm}$ (300 K), $p = 0.41$, and $R = 0.22$.

The temperature- and size-dependent resistivity values are calculated for M1, intermediate, and global wires at each technology node using (1) with ITRS dictated parameters at each technology node and with temperature-dependent parameters (ρ_o and λ) known at a given temperature. Note that only ρ_o and λ change with temperature and other scattering parameters (p and R) are independent of temperature. As temperature increases, ρ_o increases linearly and λ decreases satisfying $\rho_o \times \lambda = \text{constant}$ [16]. The calculated resistivity and its constituents are shown in Fig. 1 as a function of technology node for the ITRS intermediate wires at 300 K. In advanced technology nodes, ρ is expected to increase significantly above ρ_o mainly due to the enhanced surface and grain boundary scattering. The contribution of surface scattering and grain boundary scattering is roughly the same, but both increase with scaling. The background scattering of the electrons by phonons, electrons and defects (impurities) that contributes to ρ_o remains constant at a given temperature, independent of scaling (wire dimensions).

B. Thermal Conductivity of Low- κ Dielectrics

The low- κ dielectric materials for interlayer and intermetal dielectric (ILD and IMD) applications are expected to have much lower thermal conductivities than oxide. It is important to assess the correlation between thermal conductivity and dielectric constant in order to evaluate the tradeoff between electrical and thermal performance. While the ITRS specifies the dielectric constant of ILD (k_{ILD}) at each technology node, the thermal conductivity of ILD (K_{ILD}), one of the essential material properties for electrothermal FEM simulations, is not available. It is difficult to find a universal relationship between K_{ILD} and k_{ILD} encompassing all low- κ dielectric candidates

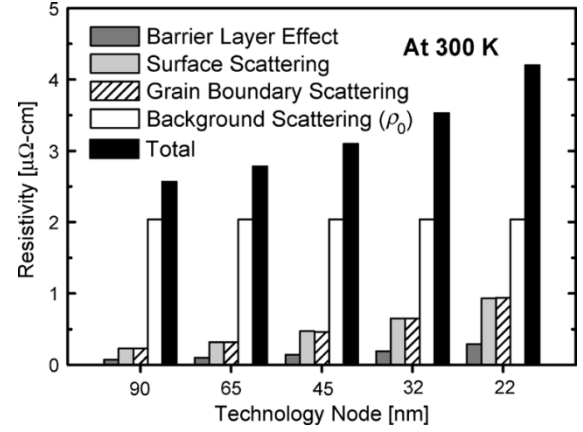


Fig. 1. Scaling of Cu resistivity for the ITRS intermediate wires at 300 K. The total resistivity is the sum of all the resistivity increments $\Delta\rho_s$, $\Delta\rho_g$, and $\Delta\rho_b$ due to surface scattering, grain-boundary scattering and barrier layer effect, plus the bulk resistivity (ρ_o). The increments, $\Delta\rho_s (= \rho_s - \rho_o)$ and $\Delta\rho_g (= \rho_g - \rho_o)$ can be easily estimated from (1) using the ITRS specified drawn wire dimensions, where the first and second terms correspond to $\Delta\rho_s$ and $\Delta\rho_g$, respectively. The increment due to barrier layer $\Delta\rho_b (= \rho_b - \rho)$ can also be estimated from (1), where ρ_b is the resistivity estimated from (1) based on the actual metal conducting dimensions excluding barrier layers and ρ is the resistivity based on the drawn wire dimensions.

owing to the intrinsic differences in their compositions and structures.

The relationship between K_{ILD} and k_{ILD} can be found if a dielectric material is porous. Using the Bruggemann effective medium theory [17], the k_{ILD} is expressed as

$$P \left(\frac{k_p - k_{\text{ILD}}}{k_p + 2k_{\text{ILD}}} \right) + (1 - P) \left(\frac{k_m - k_{\text{ILD}}}{k_m + 2k_{\text{ILD}}} \right) = 0 \quad (2)$$

where P is the porosity ($0 < P < 1$), k_p is the dielectric constant of pores, and k_m is the dielectric constant of a matrix material. The thermal conductivity of a porous dielectric material can be obtained from several models such as the parallel model, the serial model, the dilute particle model, the dilute fluid model, the porosity weighted dilute medium model, the porosity weighted simple medium (PWSM) model [18], [19], and the differential-effective-medium (DEM) model [20]. The PWSM model for K_{ILD} is given by

$$K_{\text{ILD}} = [PK_p + (1 - P)K_m](1 - P^x) + \frac{K_p K_m P^x}{PK_m + (1 - P)K_p} \quad (3)$$

where K_p is the thermal conductivity of pores, K_m is the thermal conductivity of a matrix material, and x is the fitting parameter. Calculating K_{ILD} and k_{ILD} by continuously varying P ($0 < P < 1$) numerically yields the relationship between these two properties for a given porous dielectric material.

Fig. 2 shows the correlation between thermal conductivity and dielectric constant of ILDs. The predictions based on the DEM and PWSM models for porous silicate (xerogel) films are plotted with experimental data from literature for various low- κ candidates including xerogel: fluorinated silicate glass (FSG) [21], hydrogen-silsesquioxane (HSQ) [20], [22], carbon-doped oxide (CDO) [21], [22], organic polymers [22], methyl-silsesquioxane (MSQ) [23], and xerogel [20], [24], [25]. For the ITRS specified range of dielectric constant ($k_{\text{ILD}} < 3$), the PWSM model fits better with experimental data for xerogel:

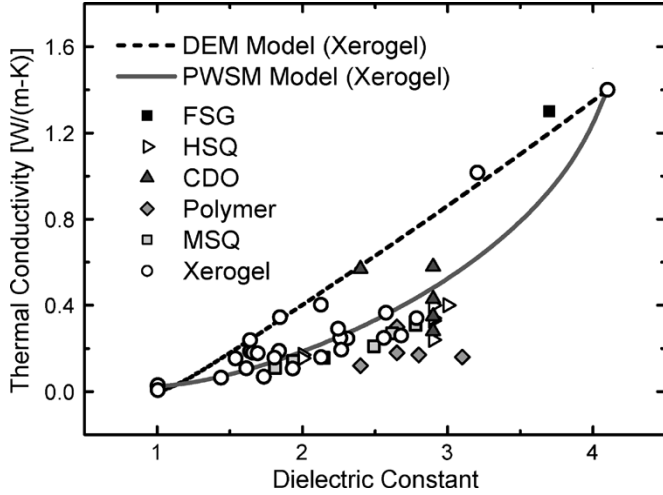


Fig. 2. Correlation between thermal conductivity and dielectric constant. The DEM and PWSM models for xerogel films are calculated using parameters $k_p = 1$, $k_m = 4.1$, $K_p = 0.0255$ W/(m-K), $K_m = 1.4$ W/(m-K), and $x = 0.49$ [18]. P is varied continuously from 0 to 1. $P = 0$ yields properties of a fully dense material (silicate) and $P = 1$ those of air.

root-mean-square-errors are 0.08 and 0.22 W/(m-K) for the PWSM and DEM models, respectively. Although the PWSM model is plotted for xerogel, it can be used as a reasonable upper bound of K_{ILD} for other low- κ dielectrics. We extracted the required K_{ILD} values corresponding to the ITRS specified bulk k_{ILD} values by using (2) and (3) with $0.357 < P < 0.668$ and parameters for xerogel.

III. FEM SIMULATIONS

A. Via Effects

The vias and contacts can be efficient heat dissipation paths from the upper level interconnects to the Si substrate and heat sink because they have much higher thermal conductivities than that of the ILD layers. On the other hand, since these electrical vias and contacts carry current, they also generate heat within their structures and increase the temperature of metal lines connected to them. Accurate estimates of interconnect temperature rise must consider these two opposite effects of vias [26]. The thermal impact of vias can be quantitatively represented by the effective thermal conductivity of ILD layers ($K_{ILD,eff}$), [7], [27]. The $K_{ILD,eff}$ value strongly depends on the via density in each ILD layer, which is typically higher for local levels and lower for global levels.

For a periodic array of metal lines and vias in Fig. 3(a), a unit cell can be defined as the volume between the symmetry planes in Fig. 3(b). Considering heat dissipation from the sides of metal lines, the effective width where thermal conduction takes place is assumed to be the entire width of the unit cell ($= w + d$), where d is the metal spacing. Constructing an equivalent 1-D thermal circuit for the unit cell results in

$$K_{ILD,eff} = f \cdot K_V + (1 - f)K_{ILD} \quad (4)$$

$$f = \frac{X^2}{[(w + d)L]} \quad (5)$$

where f ($0 < f < 1$) is the via density defined as the ratio of the via volume to the ILD volume within the unit cell, as illustrated

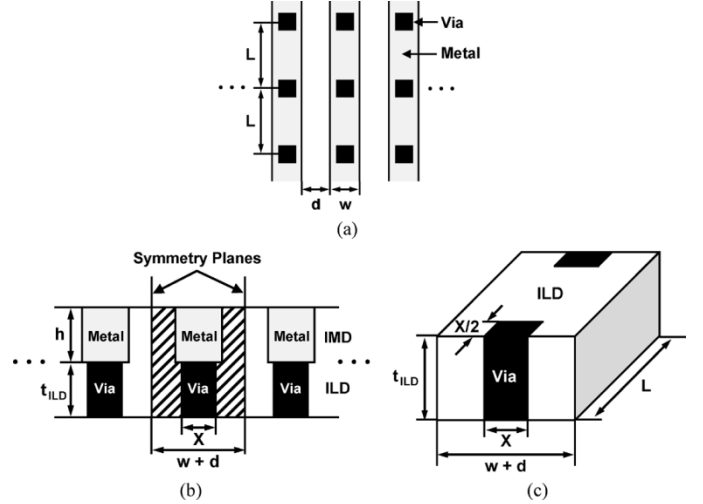


Fig. 3. Schematic of a periodic array of metal lines and vias: (a) layout, (b) cross section, and (c) the volume defining the via density.

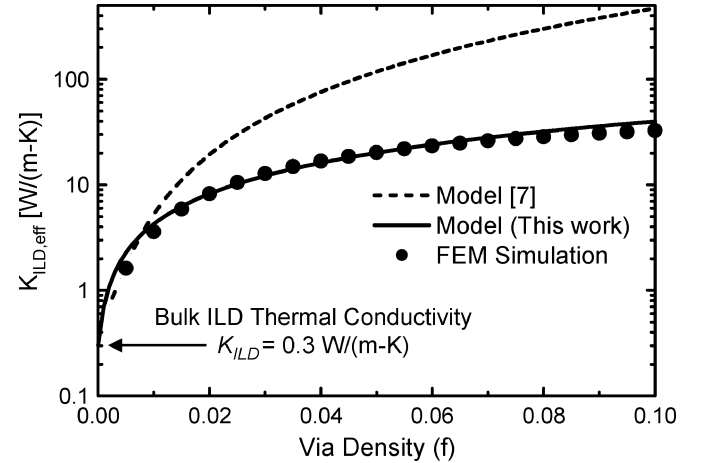


Fig. 4. Effective thermal conductivity of ILD layers ($K_{ILD,eff}$) as a function of via density (f). Simulation parameters are based on metal 1 (M1) of 65-nm technology node: $w = d = X = 76$ nm, $h = t_{ILD} = 129.2$ nm, $K_{ILD} = 0.3$ W/(m-K), $K_M = K_V = 396.36$ W/(m-K), $J = 3$ MA/cm², $\rho = 5.75$ $\mu\Omega \cdot \text{cm}$, and the reference temperature is 85 °C.

in Fig. 3(c), K_V is the via thermal conductivity, X is the via size, and L is the intervial distance along the metal line. The via size X is assumed to be the same as the minimum line width connected to the via.

In order to evaluate this analytical model for $K_{ILD,eff}$, 3-D electrothermal FEM simulations are performed for the unit cell in Fig. 3(b) with varying L . The metal line and via carry the same current, and the IMD layer is assumed to be the same as the ILD layer. Fig. 4 compares the $K_{ILD,eff}$ values extracted from FEM simulations with the predictions from thermal models as a function of f . The $K_{ILD,eff}$ values are extracted from FEM simulations by $K_{ILD,eff} = (J^2 \rho \cdot h \cdot t_{ILD}) / \Delta T_{avg}$, where J is the current density in the metal line, h is the metal height, t_{ILD} is the ILD thickness, and ΔT_{avg} is the average temperature rise of the metal line with respect to the bottom surface of the unit cell. It is shown that the $K_{ILD,eff}$ using (4), (5) fits better with the FEM simulation results. A previous model [7], which neglects heat dissipation from the sides of metal lines and heat generation in the vias themselves, significantly overestimates $K_{ILD,eff}$ especially for the higher via densities. In this paper,

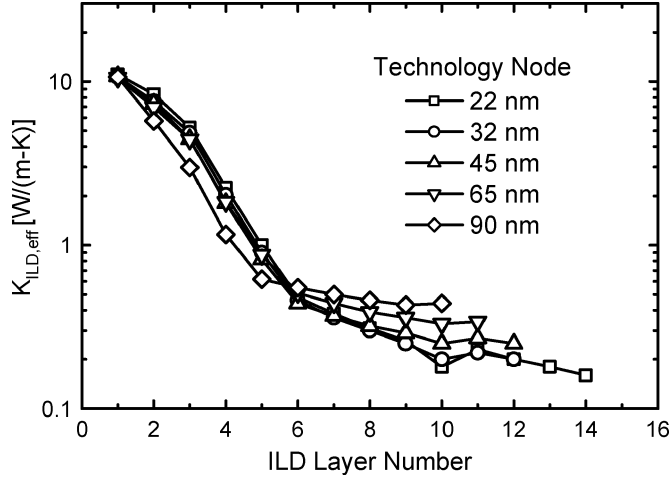


Fig. 5. Effective thermal conductivity of ILD layers ($K_{ILD,eff}$) as a function of ILD layer number for different technology nodes. The n^{th} ILD layer is defined as the ILD layer between the $(n - 1)^{\text{th}}$ and n^{th} metal levels from the substrate.

(4), (5) are used for calculating metal-level-dependent $K_{ILD,eff}$ at each technology node.

The via density (f) or intervia distance (L), which is not provided by the ITRS, varies with metal level depending on various circuit design parameters. In this work, we propose reasonable L values at successive metal levels using the following criteria. For local (M1) wires, L is taken as the typical local interconnection length which is roughly 2–3 times the source/drain diffusion length of a minimum sized NMOS. For intermediate wires, the metal wire at the center of intermediate tier (M5 for 90-nm node and M6 for the other nodes) is assumed to have an intervia distance equal to the typical length of intermediate level interconnections. For the topmost global wire, the typical interbuffer distance (hence L) for optimal delay in the longest global wires at the current technology node (90-nm node) is taken as 1 mm, and for future technology generations this length is scaled in accordance with wire width scaling. For the remaining successive metal levels, the L values are assigned by linear interpolations on a log scale.

Using these metal-level-dependent L values, the f values are calculated by using (5) assuming $d = w$, and then the $K_{ILD,eff}$ values are calculated by using (4). For the first ILD layer that is the premetal dielectric (PMD) layer, we assumed phospho silicate glass (PSG) as a PMD material and tungsten as a contact material with thermal conductivities of 0.94 W/(m-K) [28] and 165 W/(m-K) [29], respectively. In Fig. 5, it is shown that the $K_{ILD,eff}$ values of lower ILD layers become much higher than the bulk ILD thermal conductivity, $K_{ILD} = 0.12 - 0.4$ W/(m-K), due to densely embedded local vias. In the FEM simulations, these $K_{ILD,eff}$ values are parametrically assigned to each ILD layer as material properties, which effectively include vias with varying densities.

B. Package Effects

Heat dissipated from the multilevel interconnect stacks is often assumed to be removed through the Si die, integrated heat spreader (IHS) and heat sink by neglecting heat dissipation through the package layers to the printed-circuit board (PCB)

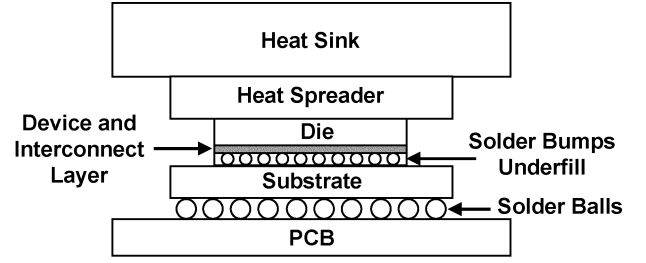


Fig. 6. Schematic of flip chip C4 package.

[11]. Fig. 6 shows schematic of a standard flip-chip controlled collapsed chip connection (C4) package. The topmost global interconnects covered by passivation layers are successively attached to the (solder bumps + underfill) layer, package substrate, solder balls, and PCB. Unlike our previous work [11], we effectively include heat dissipation through the package layers in our simulations by adding an equivalent package layer with thermal resistance of $R_{th,eq}$ to the topmost global wires

$$R_{th,eq} = \sum_i R_{th,i} = \sum_i \left(\frac{t_i}{K_i} \right) \quad (6)$$

where i represents each package layer from passivation layers to PCB, $R_{th,i}$ is the thermal resistance ($\text{mm}^2\text{K/W}$), t_i is the thickness, and K_i is the thermal conductivity of the i^{th} package layer, respectively.

For the (solder bumps + underfill) layer, the effective thermal conductivity ($K_{U,eff}$) at each technology node is calculated using the 1-D thermal circuit model and ITRS specified area array flip chip package requirements for high-performance microprocessor units (MPUs) as follows:

$$K_{U,eff} = \phi \cdot K_B + (1 - \phi)K_U \quad (7)$$

$$\phi = \frac{N_B W_B^2}{A_c} \quad (8)$$

where ϕ is the volume fraction of solder bumps ($0 < \phi < 1$), K_B is the thermal conductivity of solder bumps ($= 36$ W/(m · K) [30]), K_U is the thermal conductivity of underfill layer ($= 0.6$ W/(m · K) [30]), N_B is the number of solder bumps, W_B is the width of the solder bumps, and A_c is the chip area. The calculated $K_{U,eff}$ values are 1.41–2.57 W/(m · K), which are within the range of published values [30]–[32]. For the other package layers, we use thickness and thermal conductivity values in Table I to calculate the thermal resistance $R_{th,i}$ in each layer. The impact of (solder bumps + underfill) layer scaling is found to be negligible, overwhelmed by the huge thermal resistances of other package layers such as the solder ball/air layer and PCB. The calculated $R_{th,eq}$ values are two orders of magnitude higher than the junction-to-ambient thermal resistances (toward the heat sink). Therefore, most heat dissipated from the multilevel interconnects is expected to be removed through the Si die, IHS, and heat sink.

C. FEM Simulation Methodology

The 3-D electrothermal FEM simulations are performed by ANSYS to account for temperature-dependent Joule heating of

TABLE I
THICKNESS, THERMAL CONDUCTIVITY, AND THERMAL RESISTANCE
OF PACKAGE LAYERS

Layer	Thickness (mm)	K ($\text{Wm}^{-1}\text{K}^{-1}$)	R_{th} ($\text{mm}^2\text{K/W}$)	Reference
Passivation (TEOS)	0.001*	1.4	0.71	[21]
Passivation (SiN)	0.001*	2.23	0.45	[28]
Solder Bump	0.0762	36	2.12	[30]
Underfill	0.0762	0.6	127	[30]
Solder Bump + Underfill	0.021–0.045**	1.24–2.57	16.94–17.51	This work
	0.0762	2.6	29.31	[30]
	0.1	1.24	80.65	[31]
	0.102	0.8	127.5	[32]
Substrate	1	2	500	[30]
Solder Ball + Air gap	0.45	0.34	1323.53	[30]
PCB	1.6	0.3	5333.33	[31]

* The 2 μm of TEOS/SiN passivation layer [10] is assumed to be 1 μm thick per layer
** The thickness of the solder bumps/underfill layer is assumed to be $0.6 \times W_B$ [30].

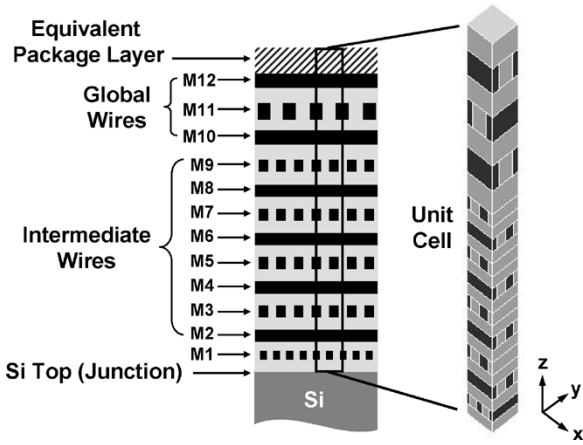


Fig. 7. FEM simulation geometry (unit cell) representing the periodic multilevel interconnect structure (45-nm technology node example).

orthogonal multilevel interconnects. The FEM simulator solves the 3-D heat diffusion equation under the steady-state

$$\frac{\partial^2 T}{\partial x^2} + \frac{\partial^2 T}{\partial y^2} + \frac{\partial^2 T}{\partial z^2} + \frac{q(T)}{K} = 0$$

where $q(T)$ is the temperature-dependent heat generation per unit volume (W/m^3) and K is the thermal conductivity of the material. For the interconnects $q(T) = J_{\text{rms}}^2 \rho(T)$ and for the other materials $q(T) = 0$, where J_{rms} is the rms current density and $\rho(T)$ is the temperature-dependent metal resistivity.

The spacing for M1 is assumed to be the same as the width of M1. The spacings for intermediate and global wires are slightly adjusted with the spacing to width ratio of 1–1.22. With adjusted spacings, the ratio of the number of M1, intermediate and global lines per unit area is found to be 4:3:2 for all technology nodes. Assuming that all metal lines are uniformly spaced with this ratio and infinitely long, a unit cell can be defined by symmetry planes as shown in Fig. 7. FEM simulations are performed for this unit cell, where four side walls satisfy symmetric (adiabatic) boundary conditions. The ITRS specified junction temperature (T_j) and ambient temperature ($T_{\text{amb}} = 45^\circ\text{C}$) are applied at the bottom of the unit cell and at the top of the equivalent package layer, respectively.

The metal-level- and technology-dependent rms current (I_{rms}) values are applied to all wires as input loads in the

TABLE II
METAL-LEVEL- AND TECHNOLOGY-DEPENDENT DUTY RATIOS

Tech. Node	90 nm	65 nm	45 nm	32 nm	22 nm
Local	0.016	0.034	0.040	0.041	0.044
Intermediate	0.132	0.158	0.175	0.182	0.180
Global (logic)	0.144	0.194	0.213	0.212	0.222
Global (clock)	0.287	0.387	0.427	0.424	0.445

electrothermal FEM simulations because interconnect Joule heating is determined by the rms current (or rms current density) as proved in Appendix I. The ITRS provides a single value of the maximum current density (J_{max}) for intermediate wires at each technology node. First, we assume that the ITRS specified J_{max} is the average current density (J_{avg}) and then calculate the average current (I_{avg}) at each technology node by $I_{\text{avg}} = J_{\text{avg}} \times A_i$, where A_i is the cross sectional area of intermediate wires. Assuming that I_{avg} is constant for all metal wires at a given technology node, the I_{rms} values are calculated by $I_{\text{rms}} = I_{\text{avg}}/r^{0.5}$, where r is the metal-level- and technology-dependent duty ratio. In this paper, the duty ratios at different metal levels and technology nodes are calculated for the first time by using SPICE simulations (Table II). It must be noted that the methodology used for the duty ratio calculation follows the same principle as that used for predicting the clock frequencies and minimum logic depths in the ITRS. The detailed methodology and assumptions are described in Appendix II. In our FEM simulations, all model dimensions, material properties, and current loads are based on the ITRS data for high performance MPUs (Table III) and incorporated as parameters in the FEM code.

IV. RESULTS AND DISCUSSION

Temperature contours within the orthogonal multilevel interconnects are obtained from fully coupled 3-D electrothermal FEM simulations. Each simulation is composed of two different cases depending on the duty ratio of global wires: 1) all global wires carry clock signals and 2) all global wires carry logic signals. In practical circuit environments, global wires can be used for both clock and logic signal transmissions. Therefore, the simulation results for these two cases can be regarded as two bounds of the predicted interconnect temperature. Fig. 8 plots the spatial chip temperature distributions along the vertical distance from the Si junction ($z = 0$) to the topmost global wires for the case with clock global wires. For 90- and 65-nm nodes, the temperature rises within the interconnect stacks are less than 13 and 33 $^\circ\text{C}$, respectively. However, metal temperatures increase significantly beyond 45-nm node owing to the combined effects of increasing metal resistivity, increasing current density, increasing number of global metal levels, and decreasing ILD thermal conductivity. The maximum metal temperature (T_{max}) occurs at the topmost global wires as indicated in the contour plot. The maximum metal temperature rise with respect to the junction temperature ($\Delta T_{\text{max}} = T_{\text{max}} - T_j$) is obtained for each simulation and used in the following thermal scaling analysis. Note that the total thickness of the (Cu + ILD) layers decreases with scaling, due to the smaller vertical dimensions of wires and insulators despite increasing number of metal levels. For the case with logic global wires, the shape of temperature profile

TABLE III
 ITRS-BASED SIMULATION PARAMETERS

		Technology Node (nm)				
		90	65	45	32	22
Wire Width (nm)	M1	107	76	54	38	27
	Intermediate	137.5	97.5	67.5	47.5	32.5
	Global	205	145	102.5	70	50
Wire Height (nm)	M1	181.9	129.2	97.2	72.2	54
	Intermediate	233.75	175.5	121.5	90.25	65
	Global	430.5	319	235.75	168	125
Wire Spacing* (nm)	M1	107	76	54	38	27
	Intermediate	147.83	105.17	76.5	53.83	39.5
	Global	223	159	113.5	82	58
ILD Thickness (nm)	M1**	181.9	129.2	97.2	72.2	54
	Intermediate	206.25	156	108	80.75	58.5
	Global	389.5	290	215.25	154	115
Number of Metal Levels***	Total	10	11	12	12	14
	M1	1	1	1	1	1
	Intermediate	7	8	8	8	8
$\rho(T_j)^*$ ($\mu\Omega\text{-cm}$)	Global	2	2	3	3	5
	M1	3.26	3.50	3.88	4.44	5.19
	Intermediate	3.08	3.24	3.57	4.00	4.66
Thermal Conductivity* ($\text{Wm}^{-1}\text{K}^{-1}$)	Global	2.88	2.97	3.15	3.44	3.81
	K_{ILD}, K_{IMD}	0.40	0.30	0.21	0.16	0.12
	$K_{ILD,eff}(\text{min})$	0.44	0.34	0.25	0.20	0.16
	$K_{ILD,eff}(\text{max})$	10.66	10.56	10.80	10.70	11.03
Barrier Layer Thickness (nm)	$K_{U,eff}$	2.57	1.86	1.70	1.58	1.41
		10	7	5	3.5	2.5
k_{ILD} (bulk)		2.7	2.4	2.1	1.9	1.7
J_{max} (MA/cm^2)		0.5	1.0	3.0	4.3	5.8
I_{avg} (mA)*		0.161	0.171	0.246	0.184	0.122
T_j ($^{\circ}\text{C}$)		90	85	85	85	85
T_{amb} ($^{\circ}\text{C}$)		45	45	45	45	45
A_c (mm^2)		310	310	310	310	310
Solder Bump Pitch (μm)		150	120	100	90	80
Solder Bump Size (μm)		75	60	50	45	40
Number of Solder Bumps****		3072	3072	3840	4224	4416
$R_{th,eq}$ ($\text{mm}^2\text{K}/\text{W}$)*		7175.54	7177.38	7175.67	7175.11	7175.05

* Calculated from this work using ITRS data.

** The ILD thickness for M1 (PMD thickness) is assumed to be the same as the height of M1.

*** The maximum numbers for intermediate and global tiers are 8 and 5, respectively.

**** The number of chip I/Os (number of total chip pads) for MPU.

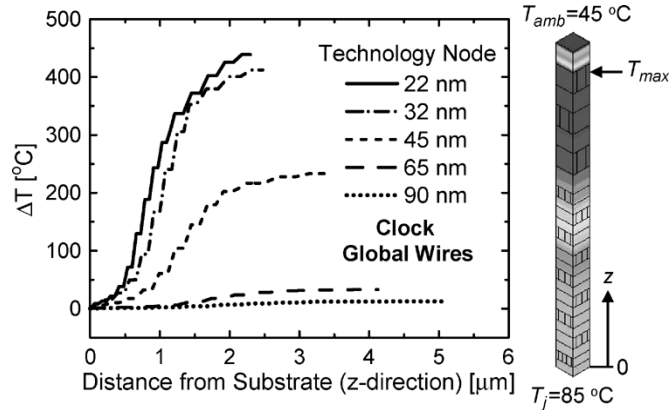


Fig. 8. Temperature rise with respect to the junction temperature ($\Delta T = T - T_j$) along the vertical distance from the Si junction (along the z direction) for the case with clock global wires. The temperature contour plot of 45-nm technology node is also shown as an example. The metal-level- and technology-dependent duty ratios are used.

is similar but the absolute temperature rise is much higher, due to smaller duty ratios (hence larger I_{rms} values) and more Joule heating: $\Delta T_{\text{max}} = 15\text{ }^{\circ}\text{C} - 906\text{ }^{\circ}\text{C}$ (from 90- to 22-nm node).

Previous thermal simulations are often based on temperature-independent simulations using constant ρ values at an arbitrary temperature (room temperature or junction temperature). Although temperature-dependent simulations using $\rho(T)$ generally require more computation times, errors induced by temperature-independent simulations must be carefully investigated.

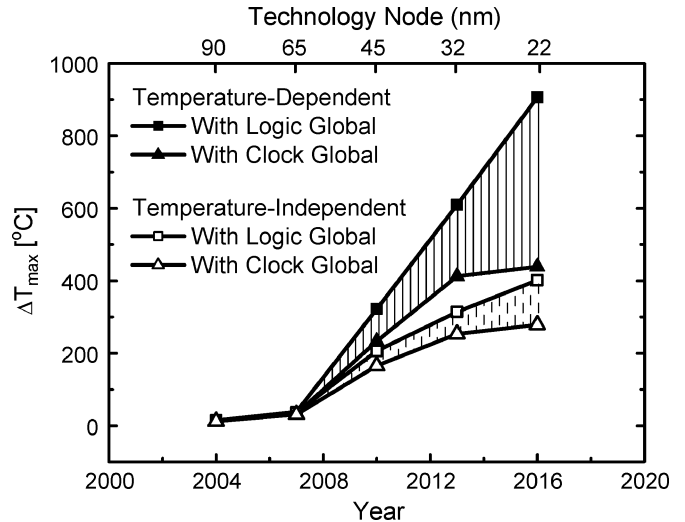


Fig. 9. Impact of temperature-dependent and temperature-independent simulations on ΔT_{max} . For temperature-independent simulations, constant ρ values at T_j are used. The size effect of ρ is included for both cases and other simulation parameters are the same.

Fig. 9 compares the predictions for ΔT_{max} from these two simulation methodologies, both of which include two cases with clock and logic global wires. As pointed out earlier, the case with clock global wires provides a lower bound of ΔT_{max} and that with logic global wires, an upper bound of ΔT_{max} . Up to 65-nm node, the temperature-dependent and -independent simulations yield almost the same results with errors less than $2\text{ }^{\circ}\text{C}$. However, beyond 45-nm node, significant underestimations of ΔT_{max} can be made by temperature-independent simulations. The temperature-dependent electrothermal simulation is shown to be necessary for accurate estimates of multilevel interconnect temperatures under aggressive thermal conditions. Furthermore, the predicted temperature range bounded by the upper and lower limits is shown to increase rapidly with scaling for the temperature-dependent simulations, which indicates that ΔT_{max} will become more sensitive to the relative fraction of logic and clock global wires in advanced technology nodes.

The contribution of various factors to the total effective resistivity has been shown in Section II-A. The contribution of these resistivity components to ΔT_{max} is compared in Fig. 10. Average ΔT_{max} values are plotted based on two cases with clock and logic global wires. The average ΔT_{max} considering all resistivity components ($\sim 670\text{ }^{\circ}\text{C}$) is much higher than that considering only bulk resistivity ($\sim 300\text{ }^{\circ}\text{C}$). If one or more resistivity components are neglected, ΔT_{max} can be significantly underestimated especially in sub-50 nm technologies. Note that the impact of barrier layers on the average ΔT_{max} is approximately the same as that of the other factors, contrary to its smallest contribution to the total resistivity (Fig. 1). The reason is that the reduced conductor cross section, by considering barrier layer, not only increases resistivity but also generates more Joule heating for a given current. The contribution of surface and grain boundary scattering to ΔT_{max} is observed to be equally important, similar to their contributions to the total resistivity.

Next, we examine the impact of ILD thermal conductivity scaling on ΔT_{max} . Fig. 11 shows that if the ILD thermal conductivity is not properly scaled in accordance with the

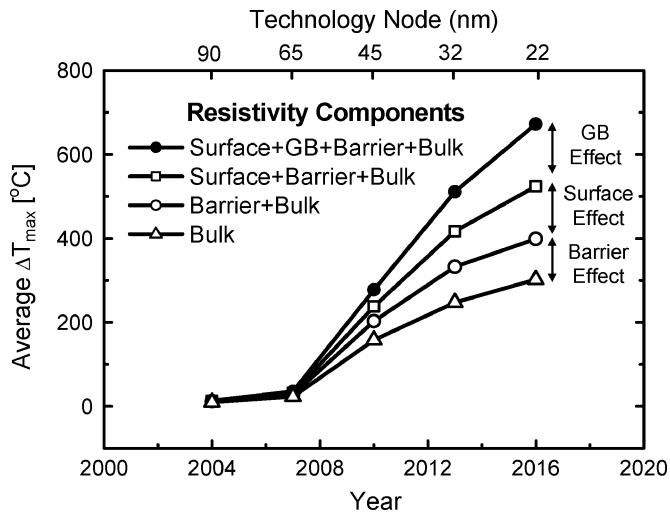


Fig. 10. Impact of resistivity scaling on average ΔT_{\max} . Note that the temperature dependence of resistivity is still considered for all cases. All other parameters are scaled with technology. GB stands for grain boundary.

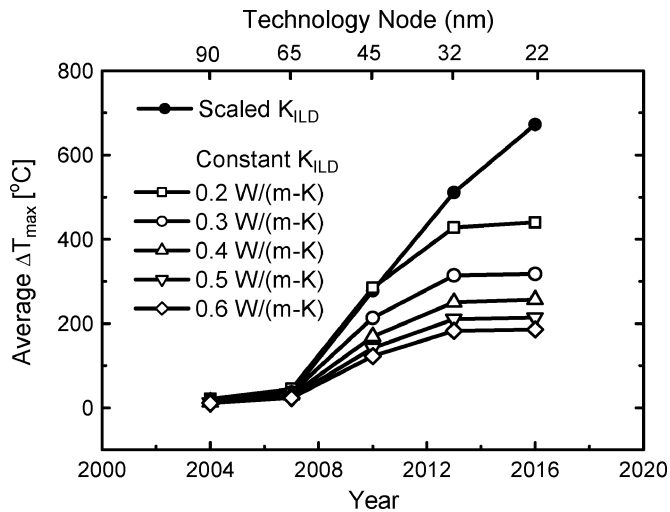


Fig. 11. Impact of ILD thermal conductivity scaling on average ΔT_{\max} . Note that the fully scaled temperature- and size-dependent resistivity values are used here. All other parameters are scaled with technology.

decreasing dielectric constant, ΔT_{\max} can be significantly underestimated. Alternatively, this plot conveys a message that if K_{ILD} can be maintained constant at 0.6 W/(m-K), average ΔT_{\max} less than 200 °C can be achieved without violating other scaling rules.

Critical parameters affecting interconnect temperatures are metal resistivity, current density, and ILD thermal conductivity. So far we have followed the ITRS-provided design rule of maximum current density (J_{\max}), which is based on scaling of device and interconnect parameters (chip frequency, gate capacitance, gate width, fanout, wire capacitance, supply voltage, etc.). However, currently manufacturable solutions are not known for $J_{\max} > 2.5 \text{ MA/cm}^2$ and for $k_{\text{ILD}} < 2.4$ that approximately corresponds to $K_{\text{ILD}} < 0.3 \text{ W/(m-K)}$. In order to provide thermal design guidelines, the contour lines of the average ΔT_{\max} are plotted in the $J_{\text{avg}} - K_{\text{ILD}}$ parameter space in Fig. 12. For lower K_{ILD} values, the average ΔT_{\max} increases more rapidly with J_{avg} indicated by the closer spacing between

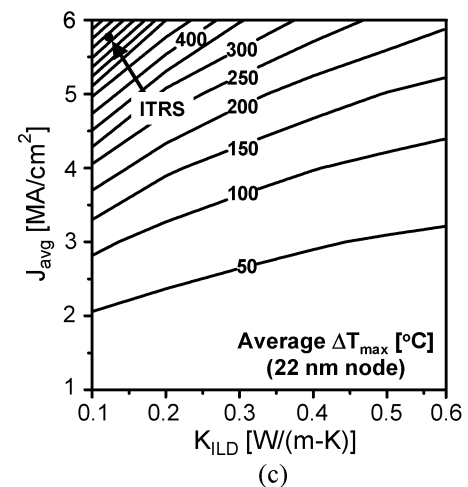
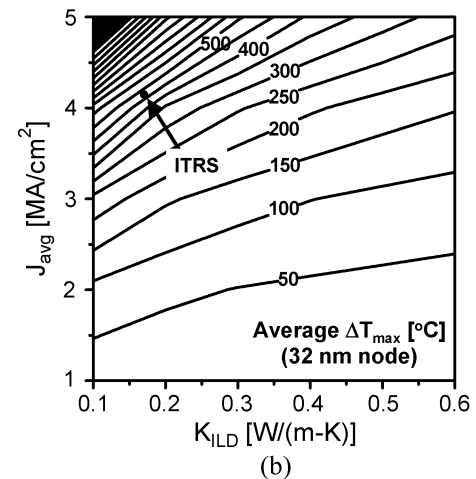
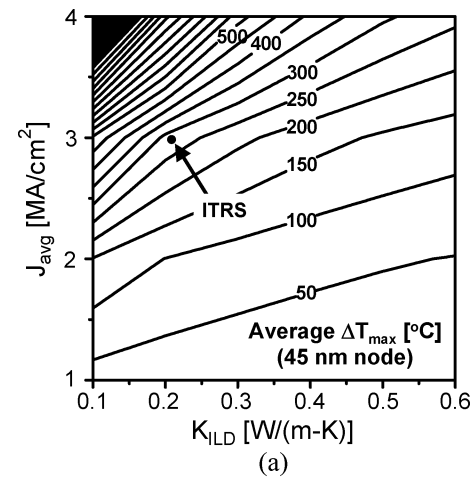


Fig. 12. Contour lines of the average ΔT_{\max} in the $J_{\text{avg}} - K_{\text{ILD}}$ parameter space for (a) 45-nm node, (b) 32-nm node, and (c) 22-nm node. The contour lines denote average ΔT_{\max} values from two cases with clock and logic global wires, increasing in steps of 50 °C. The shaded regions in (a) and (b) indicate temperature rises above the melting point of Cu ($\Delta T_{\max} > 1000 \text{ °C}$). The ITRS requirements for J_{avg} and K_{ILD} are also indicated.

isotherms. Moving toward the higher K_{ILD} values will provide more room for the current density design. Note that for the same $J_{\text{avg}} - K_{\text{ILD}}$ pair, the average ΔT_{\max} continuously decreases from 45 to 22 nm node due to increasing duty ratios (decreasing rms current and Joule heating). A proper choice of

$J_{\text{avg}} - K_{\text{ILD}}$ parameter sets can achieve reasonably low metal temperatures while still preserving other scaling trends.

V. CONCLUSION

A rigorous scaling analysis of multilevel interconnect temperatures in high performance ICs has been performed using 3-D electrothermal FEM simulations. Detailed calculations of Cu resistivity have considered various scattering mechanisms, barrier layer effect, and temperature dependence. A methodology for extracting the correlation between thermal conductivity and dielectric constant of low- κ materials has been presented based on fully physical models. In addition, an accurate thermal model has been proposed to account for the thermal impact of vias. The comprehensive scaling analysis based on fully coupled technological, structural and material factors has showed that the average maximum interconnect temperature rise is expected to be about 300–700 °C in sub-50-nm interconnect technologies. It has been shown that the interconnect Joule heating problem will become more severe due to coupled effects of increasing metal resistivity, increasing current density, and decreasing ILD thermal conductivity if other variables follow the ITRS scaling rules. Although increasing metal resistivity might be an inevitable consequence of wire dimension scaling, it could be alleviated by reducing barrier layer/Cu interface roughness (increasing p) and by reducing the grain boundary density and impurity enrichment (decreasing R). Minimizing barrier layer thickness can also be an object of further investigation. Developing nonporous low- κ dielectric materials with higher thermal conductivity and considering optimal density thermal vias during the early design phase might be other solutions to enhance heat dissipation and achieve lower interconnect temperatures.

APPENDIX I

This section provides a simple proof of why interconnect Joule heating is determined by the rms current. The rms (or the effective) value of any time-varying current (or voltage) is defined as the square root of the mean value of the squared function. For example, for a periodic current function

$$I(t) = I_0 \cos(\omega t + \phi) \quad (\text{A11})$$

the rms value of the current is given by

$$I_{\text{rms}} = \sqrt{\frac{1}{T} \int_{t_0}^{t_0+T} I^2(t) dt} = \sqrt{\frac{1}{T} \int_{t_0}^{t_0+T} I_0^2 \cos^2(\omega t + \phi) dt} \quad (\text{A12})$$

where the mean value of the current is obtained by integrating $I^2(t)$ over one time period, (i.e., from t_0 to $t_0 + T$), and then dividing by the range of integration, T .

Now consider that a periodic current (shown in (A11)) flows along an interconnect of resistance R . The average power dis-

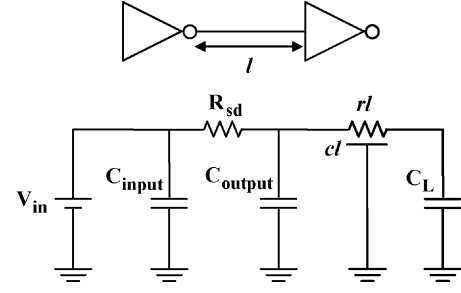


Fig. 13. Equivalent circuit diagram for an inverter driving an interconnect and a load.

sipated due to Joule heating is the average of the instantaneous power (p) over one period ($= T$), which can be expressed as

$$P_{\text{avg}}^{\text{int}} = \frac{1}{T} \int_{t_0}^{t_0+T} p dt = R \frac{1}{T} \int_{t_0}^{t_0+T} I_0^2 \cos^2(\omega t + \phi) dt. \quad (\text{A13})$$

Comparing (A12) and (A13) reveals that the average power dissipated in the interconnect of resistance R is simply the product of the rms value of the current and R

$$P_{\text{avg}}^{\text{int}} = I_{\text{rms}}^2 R. \quad (\text{A14})$$

APPENDIX II

This section describes the strategy used to evaluate typical values of duty ratio at different interconnect metal levels (local, intermediate, and global) and at different technology nodes. The duty ratio for a metal interconnection is the ratio of the time (per clock cycle) when it carries a current to the clock time period. The duty ratio is determined by various factors such as the current drive strength, the dimensions of the wire and the effective capacitive loading on the signal being driven. In this work, the typical VLSI circuit scenario of a gate driving an appropriate interconnection and a capacitive load is used to estimate the metal duty ratio by using SPICE simulations. Without any loss of generality, the driver and load are chosen to be inverter gates of appropriate sizes and fanout. The circuit and its equivalent representation for such a configuration are shown in Fig. 13.

The driver gate is represented by a voltage source and an equivalent resistance R_{sd} which corresponds to its parasitic source/drain resistance as well as the input gate capacitance. The load driven by this gate is composed of the output parasitic capacitance (junction/diffusion capacitance plus gate-overlap capacitance) of the driving gate, the $R-C$ network corresponding to the interconnection and the total input gate capacitances of the gates being driven. The relevant device/gate driver parameters are used in this work, based on ITRS predictions. The ITRS provides gate and overlap capacitances (C_{gn} and C_{ovn} , respectively) for a typical NMOS device. The corresponding figures for a minimum sized inverter are calculated by assuming a PMOS-NMOS sizing ratio of 2 (to roughly match PMOS/NMOS drive currents). Hence, the gate input capacitance is calculated as

$$C_{\text{input}} = C_{\text{gn}} + C_{\text{gp}} = 3 \cdot C_{\text{gn}}. \quad (\text{A11})$$

In calculating the parasitic output capacitance for a minimum-sized inverter, the junction capacitance of a gate is assumed to be half of its input capacitance [33]. The gate output capacitance is given by

$$C_{\text{output}} = (C_{\text{jn}} + C_{\text{jp}}) + (C_{\text{ovn}} + C_{\text{ovp}}) = \left(\frac{3}{2}C_{\text{gn}}\right) + (3 \cdot C_{\text{ovn}}). \quad (\text{AII2})$$

The gate overlap capacitance includes the worst-case Miller effect which causes an increase in the effective capacitance.

Local wires have the smallest cross section dimensions with high resistance (and capacitance) per unit length and are used for providing the interconnections between nearby gates and devices so that the length is not too long. Since these wires carry signals over short distances, the wire delay is not very high and the drivers for these signals are usually minimum sized gates so as to give minimum switching delay and hence best performance for the logic circuitry. Since local interconnections are mostly used for logic circuitry, the load capacitance is calculated assuming that it drives a fanout of four, as done in the familiar FO4 delay calculations. The typical local interconnection length is assumed to be 9λ , where λ is the layout parameter, one half of the minimum feature size for a particular technology node. The effective resistivity for Cu considers the size-dependent surface and grain boundary scatterings at T_j . Capacitance values are extracted using FastCap [34].

In the case of intermediate and global wires, the wire lengths are much longer and minimum sized drivers are not enough to drive the large loads while meeting the timing requirements. Buffers (repeaters in the form of inverters) need to efficiently drive signals over the long interconnections. These buffers have sizes much larger than the minimum sized gates. Increasing driver sizes improves their drive current, but also increases the load capacitance and hence the sizes and interbuffer separation is optimized so as to achieve minimum delay. The commonly used optimal delay buffer insertion methodology [35] is used to find appropriate driver sizes and interconnection lengths for global wires. The optimal delay interbuffer distance is found to be of the same order as the maximum interconnect length over which delay is equal to the RC delay of the interconnect ($\tau = RC$) [1]. For intermediate level interconnections, the wire length is assumed to be the same as the $\tau = RC$ length as provided by ITRS, while driver and load sizes are determined by the same procedure as for global interconnections. Unlike local wires, global and intermediate wires do not drive a fanout of four. Instead, the load is the input capacitance of the next buffer stage which is of the same size as the driver itself. For global interconnections, it is a good rule of thumb to assume the rise time of the input signal to the driver as 10% of the clock period [36]. This assumption has been applied for both intermediate and global wires in these simulations.

Other assumptions used for all these calculations are as follows. The on-time for each metal interconnection is taken as the time for which it carries a current greater than 10% of the maximum current value, for each cycle. One transition per clock cycle is assumed, which is a typical behavior for wires carrying logic signals. In the case of global wires, however, which are most often used for chip-wide communication of signals

such as the clock which obviously undergo two transitions per clock cycle, two values of duty ratio are shown—one assuming a single transition and the other assuming two transitions per clock cycle.

REFERENCES

- [1] (2003) International Technology Roadmap for Semiconductors (ITRS). [Online] Available: <http://public.itrs.net/>
- [2] K. Banerjee, A. Mehrotra, A. Sangiovanni-Vincentelli, and C. Hu, "On thermal effects in deep sub-micron VLSI interconnects," in *Proc. ACM DAC*, 1999, pp. 885–891.
- [3] K. Banerjee and A. Mehrotra, "Global (interconnect) warming," *IEEE Circuits Devices Mag.*, no. 9, pp. 16–32, Sep. 2001.
- [4] W. R. Hunter, "Self-consistent solutions for allowed interconnect current density—part II: application to design guidelines," *IEEE Trans. Electron Devices*, vol. 44, no. 2, pp. 310–316, Feb. 1997.
- [5] C. C. Teng, Y. K. Cheng, E. Rosenbaum, and S. M. Kang, "iTEM: a temperature-dependent electromigration reliability diagnosis tool," *IEEE Trans. Computer-Aided Des. Integr. Circuits Syst.*, vol. 16, no. 8, pp. 882–893, Aug. 1997.
- [6] D. Chen, E. Li, E. Rosenbaum, and S. Kang, "Interconnect thermal modeling for accurate simulation of circuit timing and reliability," *IEEE Trans. Computer-Aided Des. Integr. Circuits Syst.*, vol. 19, no. 2, pp. 197–205, Feb. 2000.
- [7] T. Y. Chiang, K. Banerjee, and K. C. Saraswat, "Analytical thermal model for multilevel VLSI interconnects incorporating via effect," *IEEE Electron Device Lett.*, vol. 23, no. 1, pp. 31–33, Jan. 2002.
- [8] Y. L. Shen, "Analysis of Joule heating in multilevel interconnects," *J. Vac. Sci. Technol. B, Microelectron. Process Phenom.*, vol. 17, no. 5, pp. 2115–2121, Sep./Oct. 1999.
- [9] X. Gui, S. K. Dew, and M. J. Brett, "Three-dimensional thermal analysis of high density triple-level interconnection structures in very large scale integrated circuits," *J. Vac. Sci. Technol. B, Microelectron. Process Phenom.*, vol. 12, no. 1, pp. 59–62, Jan./Feb. 1994.
- [10] S. Rzepka, K. Banerjee, E. Meusel, and C. Hu, "Characterization of self-heating in advanced VLSI interconnect lines based on thermal finite element simulation," *IEEE Trans. Comp., Packag., Manufact. Technol. A*, vol. 21, no. 3, Sep. 1998.
- [11] S. Im and K. Banerjee, "Full chip thermal analysis of planar (2-D) and vertically integrated (3-D) high performance ICs," in *IEDM Tech. Dig.*, 2000, pp. 727–730.
- [12] W. Steinhogel, G. Schindler, G. Steinlesberger, M. Traving, and M. Engelhardt, "Comprehensive study of the resistivity of copper wires with lateral dimensions of 100 nm and smaller," *J. Appl. Phys.*, vol. 97, no. 2, pp. 023 706-1–023 706-7, 2005.
- [13] K. Fuchs, "Conduction electrons in thin metallic films," *Proc. Cambridge Phil. Soc.*, vol. 34, p. 100, 1938.
- [14] E. H. Sondheimer, "The mean free path of electrons in metals," *Adv. Phys.*, vol. 1, no. 1, pp. 1–42, 1952.
- [15] A. F. Mayadas and M. Shatzkes, "Electrical resistivity model for polycrystalline films: The case of arbitrary reflection at external surfaces," *Phys. Rev. B, Condens. Matter*, vol. 1, no. 4, pp. 1382–1389, 1970.
- [16] W. Steinhogel, G. Schindler, G. Steinlesberger, and M. Engelhardt, "Size-dependent resistivity of metallic wires in the mesoscopic range," *Phys. Rev. B, Condens. Matter*, vol. 66, no. 7, pp. 075 414/1–075 414/4, 2002.
- [17] R. M. Azzam and N. M. Bashara, *Ellipsometry and Polarized Light*. Amsterdam, The Netherlands: Elsevier, 1977.
- [18] C. Hu, M. Morgen, P. S. Ho, A. Jain, W. N. Gill, J. L. Plawsky, and P. C. Wayner, "Thermal conductivity study of porous low- κ dielectric materials," *Appl. Phys. Lett.*, vol. 77, no. 1, pp. 145–147, 2000.
- [19] M. Kaviany, *Principles of Heat Transfer in Porous Media*. New York: Springer-Verlag, 1991.
- [20] R. M. Costescu, A. J. Bullen, G. Matamis, K. E. O'Hara, and D. G. Cahill, "Thermal conductivity and sound velocities of hydrogen-silsesquioxane low- κ dielectrics," *Phys. Rev. B, Condens. Matter*, vol. 65, no. 9, pp. 094 205/1–094 205/6, 2002.
- [21] B. C. Daly, H. J. Maris, W. K. Ford, G. A. Antonelli, L. Wong, and E. Andideh, "Optical pump and probe measurement of the thermal conductivity of low- κ dielectric thin films," *J. Appl. Phys.*, vol. 92, no. 10, pp. 6005–6009, 2002.
- [22] P. Zhou, Ph.D. dissertation, Stanford University, Stanford, CA, 2001.
- [23] J. Liu, D. Gan, C. Hu, M. Kiene, P. S. Ho, W. Volksen, and R. D. Miller, "Porosity effect on the dielectric constant and thermomechanical properties of organosilicate films," *Appl. Phys. Lett.*, vol. 81, no. 22, pp. 4180–4182, 2002.

- [24] A. Jain, S. Rogojevic, S. Ponoht, W. N. Gill, J. L. Plawsky, E. Simonyi, S. T. Chen, and P. S. Ho, "Processing dependent thermal conductivity of nanoporous silica xerogel films," *J. Appl. Phys.*, vol. 91, no. 5, pp. 3275–3281, 2002.
- [25] B. Y. Tsui, C. C. Yang, and K. L. Fang, "Anisotropic thermal conductivity of nanoporous silica film," *IEEE Trans. Electron Devices*, vol. 51, no. 1, pp. 20–27, Jan. 2004.
- [26] S. Im, K. Banerjee, and K. E. Goodson, "Modeling and analysis of via hot spots and implications for ULSI interconnect reliability," in *Proc. IRPS*, 2002, pp. 336–345.
- [27] Y. C. Lee, H. T. Ghaffari, and J. M. Segelken, "Internal thermal resistance of a multichip packaging design for VLSI based systems," *IEEE Trans. Comp., Hybrids, Manufact. Technol.*, vol. 12, no. 2, pp. 163–169, Jun. 1989.
- [28] M. von Arx, O. Paul, and H. Baltes, "Process-dependent thin-film thermal conductivities for thermal CMOS MEMS," *J. Microelectromech. Syst.*, vol. 9, no. 1, pp. 136–145, Mar. 2000.
- [29] F. P. Incropera and D. P. DeWitt, *Fundamentals of Heat and Mass Transfer*. New York: Wiley, 1996.
- [30] T. Y. Lee, "An investigation of thermal enhancement on flip chip plastic BGA packages using CFD tool," *IEEE Trans. Comp. Packag. Technol.*, vol. 23, no. 3, pp. 481–489, Sep. 2000.
- [31] S. N. Towle, H. Braunisch, C. Hu, R. D. Emery, and G. J. Vandentop, "Bumpless build-up layer packaging," in *Proc. ASME Int. Mech. Eng. Congress and Exposition (IMECE)*, 2001, EPP-24 703.
- [32] J. Parry, H. Rosten, and G. B. Kromann, "The development of component-level thermal compact models of a C4/CBGA interconnect technology: The Motorola PowerPC 603 and PowerPC 604 RISC microprocessors," *IEEE Trans. Comp., Packag., Manufact. Technol. A*, vol. 21, no. 1, pp. 104–112, Mar. 1998.
- [33] R. Ho, K. W. Mai, and M. A. Horowitz, "The future of wires," *Proc. IEEE*, vol. 89, no. 4, pp. 490–504, Apr. 2001.
- [34] K. Nabors and J. White, "FastCap: a multipole accelerated 3-D capacitance extraction program," *IEEE Trans. Computer-Aided Des. Integr. Circuits Syst.*, vol. 10, no. 11, pp. 1447–1459, Nov. 1991.
- [35] H. B. Bakoglu, *Circuits Interconnections, and Packaging for VLSI*. Reading, MA: Addison-Wesley, 1990.
- [36] C.-K. Cheng, J. Lillis, S. Lin, and N. Chang, *Interconnect Analysis and Synthesis*. New York: Wiley, 2000.



Sungjun Im (S'02) received the B.S. degree in metallurgical engineering from Seoul National University, Seoul, Korea, in 1998, and the M.S. degree in materials science and engineering from Stanford University, Stanford, CA, in 2001, where he is currently pursuing the Ph.D. degree in the Department of Materials Science and Engineering. His doctoral research is being jointly supervised by Prof. K. Goodson (Mechanical Engineering Department, Stanford University) and Prof. K. Banerjee (Electrical and Computer Engineering Department,

University of California, Santa Barbara).

His research interests include nanoscale conduction heat transport phenomena, interconnect reliability and performance optimization in high-performance VLSI and 3-D ICs, and development of cooling technologies for integrated heterogeneous circuits and systems.

Mr. Im received the Outstanding Student Paper Award at the 2005 VLSI/ULSI Multilevel Interconnection Conference.



Navin Srivastava (S'03) received the B. Tech. (honors) degree in electrical engineering from the Indian Institute of Technology, Kharagpur, India, in 2000. He is currently pursuing the Ph.D. degree in electrical and computer engineering at the University of California, Santa Barbara, under the supervision of Prof. K. Banerjee.

He has worked in the Electronic Design Automation industry for three years. His research interests are in the modeling and analysis of high-frequency-effects in VLSI interconnects as well as modeling of

carbon nanotube interconnects.

Mr. Srivastava received the Outstanding Student Paper Award at the 2005 VLSI/ULSI Multilevel Interconnection Conference.



Kaustav Banerjee (S'92–M'99–SM'03) received the Ph.D. degree in electrical engineering and computer sciences from the University of California at Berkeley, in 1999.

In July 2002, he joined the Faculty of the Department of Electrical and Computer Engineering, University of California, Santa Barbara (UCSB), where he is currently an Associate Professor. He was with Stanford University, Stanford, CA, from 1999 to 2002 as a Research Associate at the Center for Integrated Systems. From February 2002 to August

2002 he was a Visiting Faculty at the Circuit Research Labs of Intel, Hillsboro, OR. In the past, he has also held summer/visiting positions at Texas Instruments Inc., Dallas, TX, and the Swiss Federal Institute of Technology (EPFL), Lausanne, Switzerland. His present research interests focus on nanometer scale issues in high-performance VLSI as well as on circuits and systems issues in emerging nanoelectronics. His research has been chronicled in over 100 journal and refereed conference papers. He has also co-edited a book titled *Emerging Nanoelectronics: Life with and after CMOS* (Springer—Verlag, 2004) and coauthored a book chapter.

Dr. Banerjee serves or has served on the technical program committees of the IEDM, IRPS, EOS/ESD Symposium, ISQED and ISPD. He has also served on the organizing committee of ISQED, at various positions including Technical Program Chair (2002) and General Chair (2005). At present, he serves on the IEEE EDS Nanotechnology Committee. He has received a number of awards in recognition of his work, including the ACM SIGDA Outstanding New Faculty Award (2004), a Research Award from the Electrostatic Discharge Association (2005), a Best Paper Award at the Design Automation Conference (2001) and an Outstanding Student Paper Award at the 2005 VLSI/ULSI Multilevel Interconnection Conference.



Kenneth E. Goodson (M'95–A'96) received the B.S. degree in mechanical engineering and the humanities, and the M.S. and Ph.D. degrees in mechanical engineering from the Massachusetts Institute of Technology (MIT), Cambridge, in 1989, 1991, and 1993, respectively.

Currently, he is an Associate Professor with the Mechanical Engineering Department at Stanford University, Stanford, CA. Prior to joining the Stanford faculty in 1994, he was with the Materials Research Group at Daimler-Benz AG on power

transistor design. At Stanford, his research group currently includes 18 students and research associates. Research activities of the group include studies of thermal transport phenomena at very small length and time scales, in particular those relevant to the design of transistors, semiconductor lasers, and MEMS; two-phase microchannel and micro-jet impingement cooling technology for semiconductor chips; and the applications of MEMS technology for biomedical diagnostics, thermal machining, and infrared imaging. He has authored or coauthored more than 100 journal and conference papers and five book chapters. He is a co-founder and former CTO of Cooligy, which develops electro-osmotic microcooling technology for computers.

Dr. Goodson has received a number of awards in recognition of his work, including the ONR Young Investigator Award, the NSF CAREER Award, the Journal of Heat Transfer Outstanding Reviewer Award (1999), a JSPS Visiting Professorship at the Tokyo Institute of Technology (1996), as well as Best Paper Awards at SEMI-THERM (2001), the VLSI/ULSI Multilevel Interconnect Conference (1998 and 2005), and SRC TECHCON (1998).